**Supplementary Information for**

# Visible-to-near-infrared photodetectors based on $SnS/SnSe_2$ and $SnSe/SnSe_2$ p–n heterostructures with a fast response speed and high normalized detectivity

*Xinfa Zhu[1], Weishuai Duan[1], Xiancheng Meng[1], Biao He[1], Yonghui Zhang[1], Pengyu Zhou[2, ✉], Mengjun Wang[1], Hongxing Zheng[1], and Chao Fan[1,✉]*

[1] School of Electronic and Information Engineering, Hebei University of Technology, Tianjin, 300401, China

[2] School of Science, Northeast Electric Power University, Jilin, 132012, China

✉Correspondence to: Pengyu Zhou, 20162715@neepu.edu.cn; Chao Fan, fanch@hebut.edu.cn

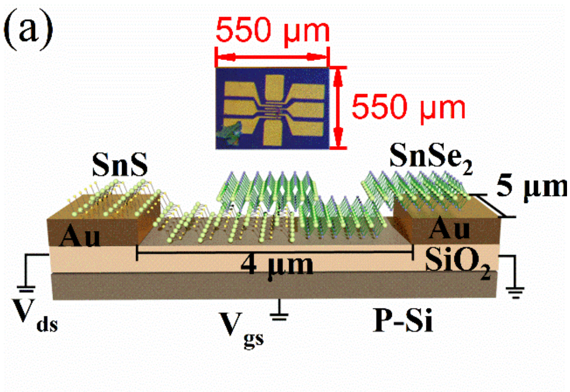


Fig. S1 (a) Diagram of the photodetector based on $SnS/SnSe_2$ heterostructure.

Fig. S1 (a) shows the diagram of the photodetector and the size of the device is nearly 550 × 550 μm$^2$.

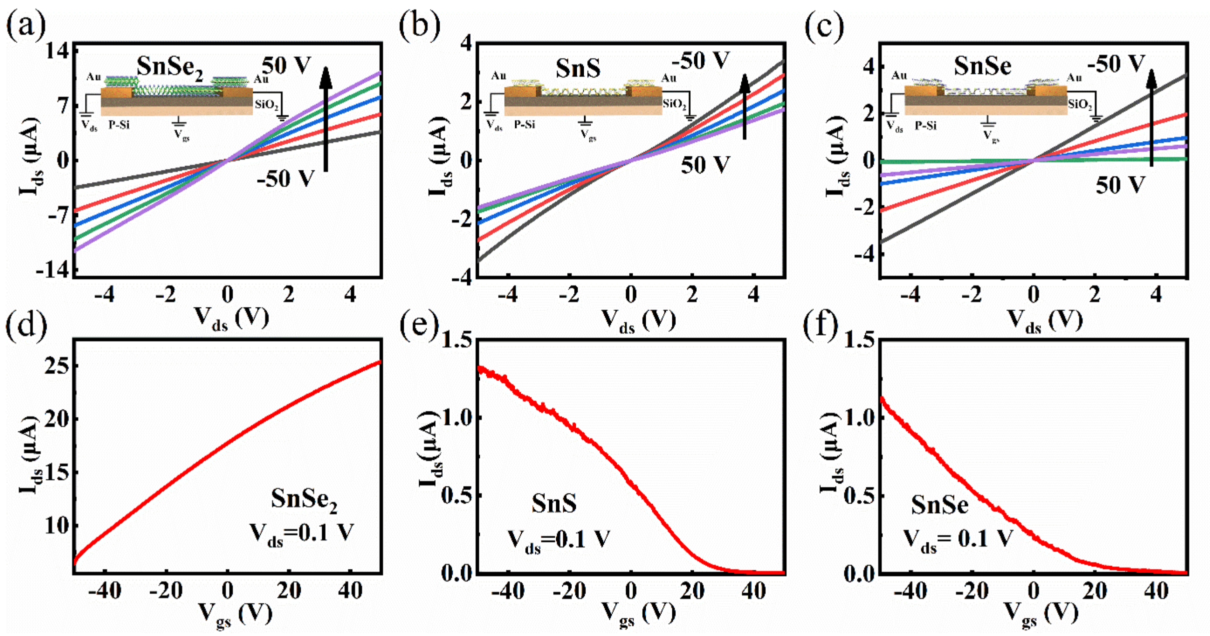


Fig. S2. Output curves of photodetectors based on $SnSe_2$ (a), SnS (b), and SnSe (c). Transfer curves of photodetectors based on $SnSe_2$ (d), SnS (e), and SnSe (f). Schematic images are shown in the insets.

The electrical characteristics of the photodetectors based on individual materials were investigated. Figs. S2 (a–c) shows the output curves of photodetectors based on $SnSe_2$, SnS, and SnSe, respectively. The output curves show good linearity, implying a good ohmic contact between samples and Au electrodes. The transfer curves of photodetectors based on $SnSe_2$, SnS, and SnSe are shown in Figs. S2 (d–f). For $SnSe_2$, the drain–source current ($I_{ds}$) increases with the increase of $V_{gs}$, indicating that $SnSe_2$ thin films show n–type behavior. Additionally, SnS and SnSe thin films exhibit p–type behaviors. The mobility values of photodetectors based on $SnSe_2$, SnS, and SnSe were estimated to be 10, 5.29, and 6.84 cm$^2$ V$^{-1}$ s$^{-1}$.

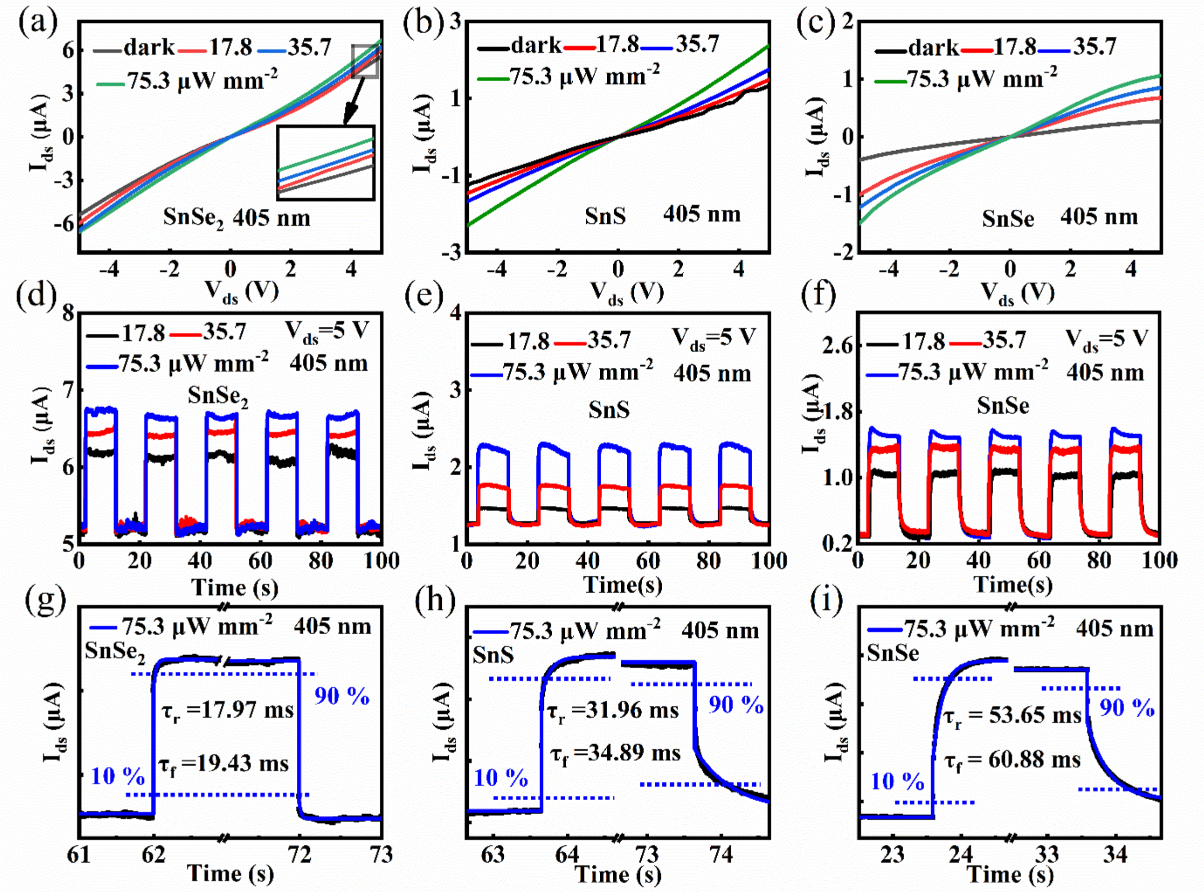


Fig. S3. photodetection performance of photodetectors based individual materials under the illumination of 405 nm. Current–voltage curves of photodetectors based on $SnSe_2$ (a), SnS (b), and SnSe (c). Transient photoresponse of photodetectors based on $SnSe_2$ (d), SnS (e), and SnSe (f). Response time of photodetectors based on $SnSe_2$ (g), SnS (h), and SnSe (i).

The photodetection performance of photodetectors based on $SnSe_2$, SnS, and SnSe under the illumination of 405 nm were detected. Figs. S3 (a–c) shows the current–voltage ($I_{ds}$–$V_{ds}$) curves of photodetectors based on individual materials with different power densities of 17.8, 35.7, 75.3 μW $mm^{-2}$. As the light power density increased, $I_{ds}$ increased simultaneously. Figs. S2 (d–f) presents the current–time ($I_{ds}$–$T$) curves of such photodetectors at $V_{ds}$ = 5 V. As photodetectors were exposed to illumination, the current increased to saturation. While the laser was turned off, the current decayed immediately to the initial state. The response time of such photodetectors was shown in Figs. S3 (g–i). The response time including the rise time $\tau_r$ and fall time $\tau_f$ were estimated as 17.97/19.43 ms ($SnSe_2$), 31.96/34.89 ms (SnS), and 53.65/60.88 ms (SnSe).

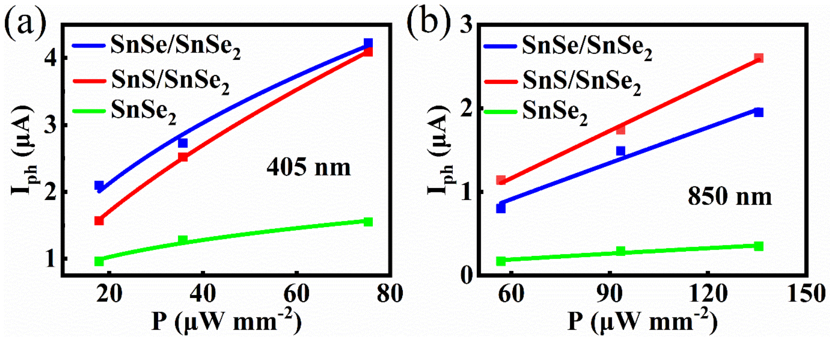


Fig. S4. Photocurrent as a function of optical power density under the illumination of 405 (a) and 850 nm (b).

Fig. S4 depicts the relationship between photocurrent and optical power density. Under the 405 nm illumination, the α values were estimated to be 0.69 and 0.60 for the $SnSe_2$/SnS and $SnSe_2$/SnSe photodetector, which are larger than that of the photodetector based on the $SnSe_2$ thin layers (0.32). Similarly, under the 850 nm illumination, the α values of $SnSe_2$/SnS (0.97) and $SnSe_2$/SnSe (0.95) photodetector are also larger than that of $SnSe_2$–based photodetectors (0.77), revealing the enhanced photocurrent conversion efficiency.

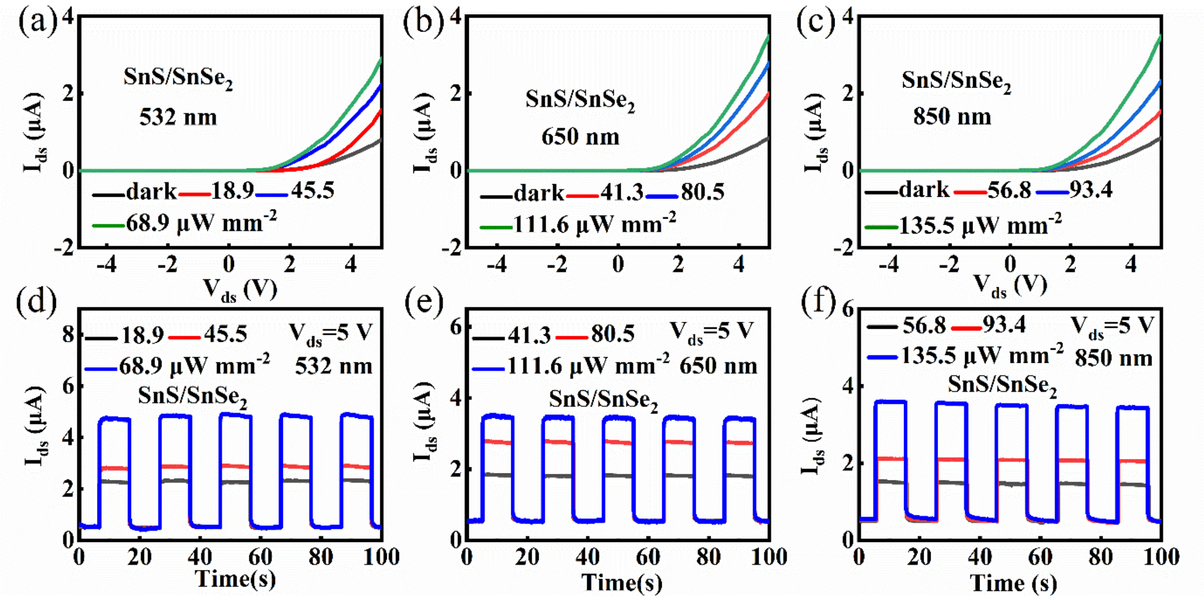


Fig. S5. photodetection performance of SnS/$SnSe_2$ photodetectors under the illumination of different wavelengths. Current–voltage curves of SnS/$SnSe_2$ photodetectors to 532 (a), 650 (b), and 850 nm (c). Transient photoresponse of SnS/$SnSe_2$ photodetectors to 532 (d), 650 (e), and 850 nm (f).

The photodetection performance of SnS/$SnSe_2$ photodetectors under the illumination of different wavelengths were detected. Figs. S5 (a–c) shows the current–voltage ($I_{ds}$–$V_{ds}$) curves of SnS/$SnSe_2$ photodetectors under the illumination of 532, 650, and 850 nm. The photodetectors exhibited an excellent broad–spectrum photodetection performance in the region from 532 nm to 850 nm. Figs. S5 (d–f) presents the current–time ($I_{ds}$–$T$) curves of SnS/$SnSe_2$ photodetectors with different wavelength. The bias voltage was set at 5 V. As can be seen that currents could alternate between saturation and initial state rapidly. And photocurrents increased multiplicatively as the light power density increased.

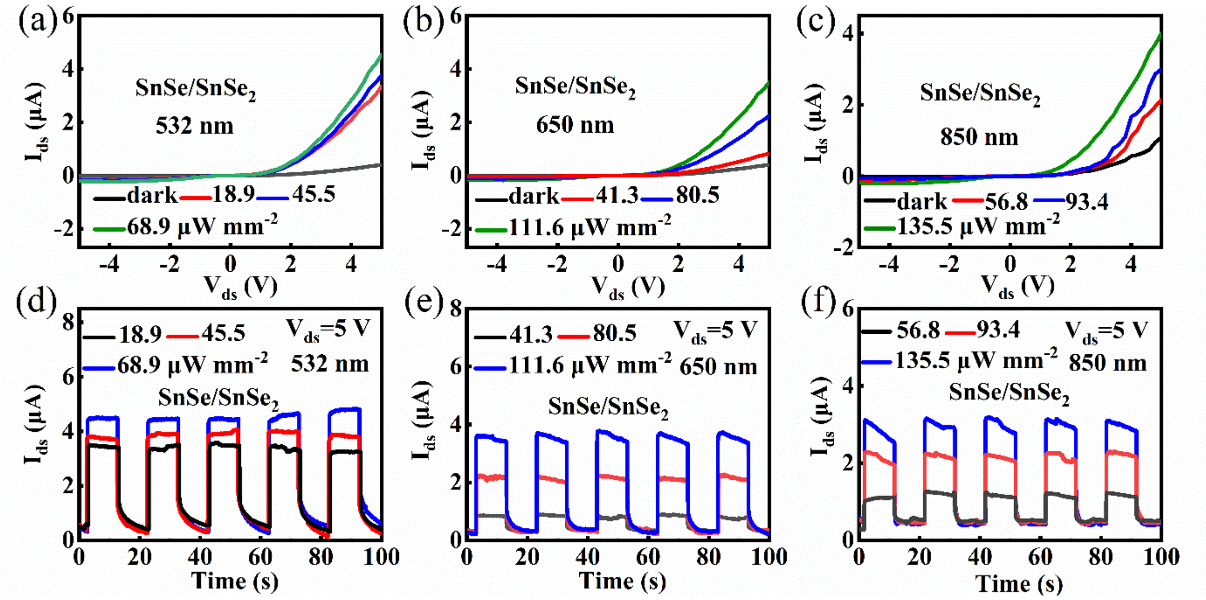


Fig. S6. photodetection performance of $SnSe/SnSe_2$ photodetectors under the illumination of different wavelengths. $I_{ds}$–$V_{ds}$ curves of $SnSe/SnSe_2$ photodetectors to 532 (a), 650 (b), and 850 nm (c). $I_{ds}$–$T$ curves of $SnSe/SnSe_2$ photodetectors to 532 (d), 650 (e), and 850 nm (f).

The photodetection performance of $SnSe/SnSe_2$ photodetectors under the illumination of different wavelengths were detected. Figs. S6 (a–c) presents the $I_{ds}$–$V_{ds}$ curves of $SnSe/SnSe_2$ photodetectors under the illumination of 532, 650, and 850 nm. The $SnSe/SnSe_2$ photodetectors also showed an excellent photodetection performance in the region from 532 nm to 850 nm. Figs. S6 (d–f) plots the $I_{ds}$–$T$ curves of $SnS/SnSe_2$ photodetectors with different wavelength. The photodetectors based on $SnS/SnSe_2$ also exhibit an instant response to the broad–spectrum illumination.

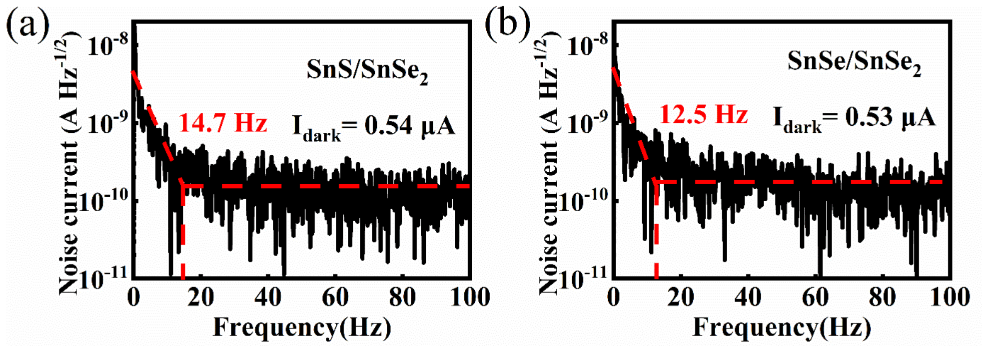


Fig. S7. Noise currents of photodetectors based on $SnS/SnSe_2$ (a) and $SnSe/SnSe_2$ (b).

As shown in Figs. S7 (a) and (b), the noise currents of the $SnS/SnSe_2$ and $SnSe/SnSe_2$ photodetectors can be derived from the fast Fourier transform of the dark current[1]. In general, the photodetector noise consists of the flicker noise (1/f noise), thermal noise, and shot noise[2]. At the frequency below 14.7 Hz (12.5 Hz), the noise current is mainly flicker noise and has a linear relationship with the frequency. At the high frequency above 14.7 Hz (12.5 Hz), the noise current is dominated by the thermal noise and shot noise dominate.

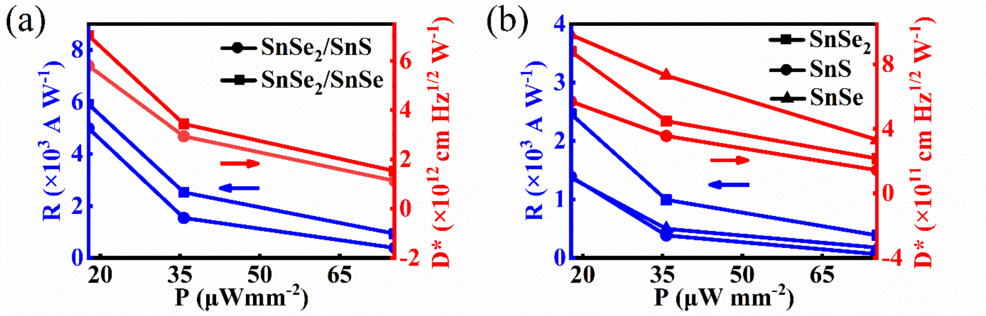


Fig. S8. Responsivity (a) and normalized detectivity (b) as a function of the power intensity of the 405 nm illumination.

Figs. S8 (a) and (b) show the responsivity ($R$) and normalized detectivity ($D^*$) as a function of the power intensity of the 405 nm illumination. The responsivity and normalized detectivity decrease with the increase of the light power intensity. The maximum $R$ values of the SnS/$SnSe_2$ and SnSe/$SnSe_2$ photodetectors were determined to be 4.99 × $10^3$ and 5.91 × $10^3$ A $W^{-1}$, respectively, which are significantly higher than that of photodetectors based on individual $SnSe_2$ (2.46 × $10^3$ A $W^{-1}$), SnS (1.19 × $10^3$ A $W^{-1}$), and SnSe (1.37 × $10^3$ A $W^{-1}$). The $D^*$ values of the SnS/$SnSe_2$ and SnSe/$SnSe_2$ photodetectors were determined to be 5.78 × $10^{12}$ and 7.03 × $10^{12}$ cm $Hz^{1/2}$ $W^{-1}$, which are one order of magnitude higher than that of photodetectors based on individual $SnSe_2$ (8.79 × $10^{11}$ cm $Hz^{1/2}$ $W^{-1}$), SnS (5.69 × $10^{11}$ cm $Hz^{1/2}$ $W^{-1}$), and SnSe (9.82 × $10^{11}$ cm $Hz^{1/2}$ $W^{-1}$).

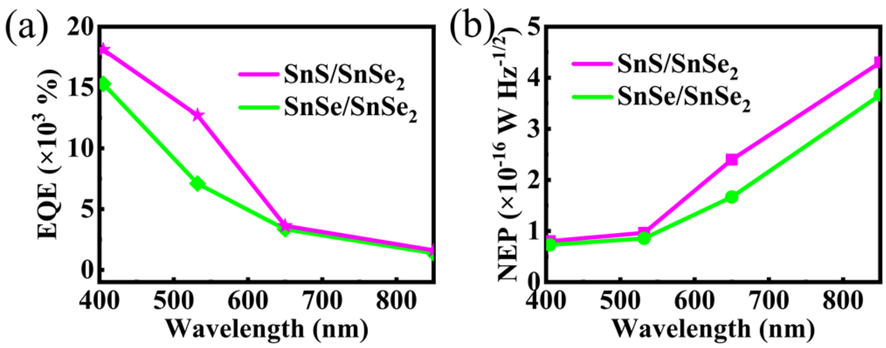


Fig. S9. External quantum efficiency (a) and noise equivalent power (b) as a function of the wavelength.

Fig. S9 (a) shows the external quantum efficiency ($EQE$) as a function of the wavelength. The external quantum efficiency decreased with the increase of the wavelength. The maximum $EQE$ values of the SnS/$SnSe_2$ and SnSe/$SnSe_2$ photodetectors were determined to be 1.53×$10^4$% and 1.81×$10^4$%, respectively. Fig. S9 (b) presents the noise equivalent power ($NEP$) as a function of the wavelength. The noise equivalent power increased with the increase of the wavelength. The minimum $NEP$ values of the SnS/$SnSe_2$ and SnSe/$SnSe_2$ photodetectors were determined to be 8.02 ×$10^{-5}$ and 7.29 × $10^{-5}$ pW $Hz^{1/2}$, respectively.

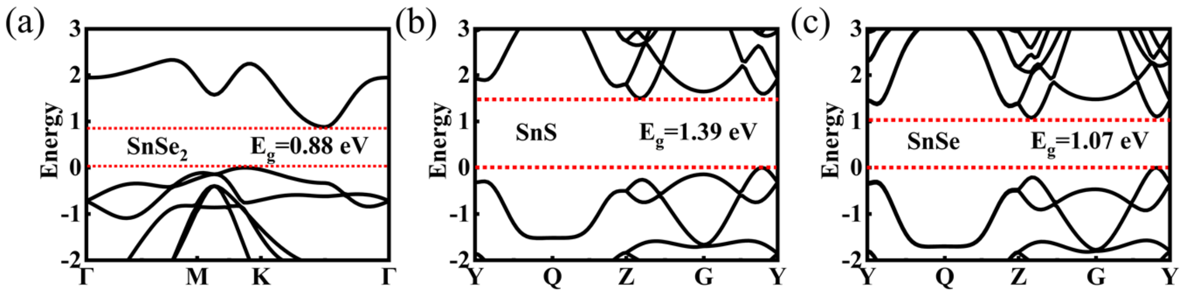


Fig. S10. Band structures of the $SnSe_2$ (a), SnS (b), and SnSe (c).

Furthermore, first–principles calculations based on the density function theory (DFT) were performed using the Vienna Ab–initio Simulation Package (VASP) [3]. The generalized gradient approximation (GGA) in the form of Perdew–Burke–Ernzerhof (PBE) was used to illustrate the exchanged–related effects. A vacuum space of 15 Å were used to avoid artificial interactions. The cut–off energy was set to 400 eV for all calculations. The Grimme DFT-D3 scheme was adopted to account for the van der Waals (vdW) interactions [4][5]. Energy and force convergence criteria was set to $10^{-5}$ eV and $10^{-3}$ eV/Å for the structural optimization. The work function difference between $SnSe_2$ and SnS is 1.67 eV, which is less than that between $SnSe_2$ and SnSe (1.73 eV). As shown in Figs. 10 (a–c), the bandgap of $SnSe_2$, SnS, and SnSe were calculated to be 0.88, 1.39, and 1.07 eV, respectively.

**Tab. S1**. A comparison of the photodetecting performance

| | $\lambda$(nm) | $R$ (A $W^{-1}$) | $D^*$ (cm $Hz^{1/2}$ W) | $\tau_r / \tau_f$ (ms) | Reference |
|---|---|---|---|---|---|
| $SnSe_2$ | 405 | 2460.3 | $8.79\times10^{11}$ | 17.97 | This work |
| SnS | 405 | 1390.0 | $5.69\times10^{11}$ | 31.96 | This work |
| SnSe | 405 | 1371.8 | $9.82\times10^{11}$ | 53.65 | This work |
| $SnS/SnSe_2$ | 405 | 4990.3 | $5.80\times10^{12}$ | 3.13 | This work |
| | 532 | 4230.2 | $4.84\times10^{12}$ | 4.98 | |
| | 650 | 1750.1 | $1.73\times10^{12}$ | 7.22 | |
| | 850 | 939.3 | $1.02\times10^{12}$ | 8.76 | |
| $SnSe/SnSe_2$ | 405 | 5912.3 | $7.03\times10^{12}$ | 4.74 | This work |
| | 532 | 5451.8 | $5.81\times10^{12}$ | 6.12 | |
| | 650 | 1890.2 | $1.63\times10^{12}$ | 8.49 | |
| | 850 | 1102.4 | $8.38\times10^{11}$ | 10.37 | |
| $WSe_2/MoS_2$ | 532 | 2700 | $5.00\times10^{11}$ | 17 | ref.[6] |
| SnTe/Ge | 808 | 0.62 | $2.33\times10^{10}$ | 206 | ref.[7] |
| $SnSe_2/MoS_2$ | 500 | 9100 | $9.3\times10^{10}$ | 200 | ref.[8] |
| $SnSe_2/WSe_2$ | 532 | 588 | $4.4\times10^{10}$ | 16 | ref.[9] |
| $PbSe/MoS_2$ | 808 | 19.7 | $2.65\times10^{10}$ | 720 | ref.[10] |
| $Gr/SnSe_2/Gr$ | 532 | 1300 | $1.48\times10^{12}$ | 30.2 | ref.[11] |
| PbSe QDs/ZnO | 808 | 0.97 | $1.86\times10^{11}$ | 340 | ref.[12] |
| $ZnIn_2S_4/Si$ | 808 | 0.50 | $2.00\times10^{12}$ | 29 | ref.[13] |
| $Bi_2Te_3/Si$ | 635 | 1 | $2.50\times10^{11}$ | 100 | ref.[14] |
| $MoS_2$/SiNWs | 450 | 2.98 | $2.70\times10^{11}$ | 450 | ref.[15] |
| $MoS_2$/CuPc | 500 | 3000 | $2\times10^{10}$ | 0.44 | ref.[16] |

# Reference:


[1] Wang W, Zhao D, Zhang F, et al. Highly sensitive low-bandgap perovskite photodetectors with response from ultraviolet to the near-infrared region. Adv. Funct. Mater, 2017, 27(42): 1703953

[2] Gong X, Tong M, Xia Y, et al. High-detectivity polymer photodetectors with spectral response from 300 nm to 1450 nm. Science, 2009, 325(5948): 1665

[3] P.-F. Loos, Exchange functionals based on finite uniform electron gases. J.Chem. Phys, 2017, 146(11): 114108

[4] Qin X Q, Dai L, Li H B, et al. Enhanced HER catalysis based on MXene/N-doped graphene heterostructures: A first-principles study. Int. J. Hydrog. Energy, 2022, 47(35): 15775

[5] Grimme S, Antony J, Ehrlich S, et al. consistent and accurate ab initio parametrization of density functional dispersion correction (DFT-D) for the 94 elements H-Pu. J Chem Phys 2010, 132:154104

[6] Shin G H, Park C, Lee K J, et al. Ultrasensitive phototransistor based on $WSe_2$-$MoS_2$ van der Waals heterojunction. Nano Letters, 2020, 20(8): 5741

[7] Song L, Tang L, Hao Q, et al. Broadband photodetector based on SnTe nanofilm/n-Ge heterostructure. Nanotechnology, 2022, 33(42): 425203

[8] Zhou X, Zhou N, Li C, et al. Vertical heterostructures based on $SnSe_2$/$MoS_2$ for high performance photodetectors. 2D Mater, 2017, 4(2): 025048

[9] Xue H, Dai Y, Kim W, et al. High photoresponsivity and broadband photodetection with a band-engineered $WSe_2$/$SnSe_2$ heterostructure. Nanoscale, 2019, 11(7): 3240

[10] Peng M, Tao Y, Hong X, et al. One-step synthesized PbSe nanocrystal inks decorated 2D $MoS_2$ heterostructure for high stability photodetectors with photoresponse extending to near-infrared region. J. Mater. Chem. C, 2022, 10(6): 2236

[11] Gao W, Zheng Z, Li Y, et al. High performance tin diselenide photodetectors dependent on thickness: a vertical graphene sandwiched device and interfacial mechanism. Nanoscale, 2019, 11(28): 13309

[12] Peng M, Liu Y, Li F, et al. Room-temperature direct synthesis of PbSe quantum dot inks for high-detectivity near-infrared photodetectors. ACS Appl. Mater. Interfaces, 2021, 13(43): 51198

[13] Zheng Z, Yao J, Li W, et al. Fabrication of a high performance $ZnIn_2S_4$/Si heterostructure photodetector array for weak signal detection. J. Mater. Chem. C, 2018, 6(47): 12928

[14] Yao J, Shao J, Wang Y, et al. Ultra-broadband and high response of the $Bi_2Te_3$-Si heterojunction and its application as a photodetector at room temperature in harsh working environments. Nanoscale, 2015, 7(29): 12535

[15] Sharmila B, Dwivedi P. $MoS_2$/SiNWs heterostructure based repeatable and highly responsive photodetector. Opt. Mater, 2022, 133: 112918

[16] Xu Z H, Tang L, Zhang S W, et al. 2D $MoS_2$/CuPc heterojunction based highly sensitive photodetectors through ultrafast charge transfer. Mater. Today Phys, 2020, 15: 100273